

PAPER • OPEN ACCESS

Solving the phase problem of diffraction: x-ray standing wave imaging on bismuthene/SiC(0001)

To cite this article: Niclas Tilgner et al 2025 2D Mater. 12 045020

View the article online for updates and enhancements.

You may also like

- Understanding domain reconstruction of twisted transition metal dichalcogenide bilayers through machine learned interatomic potentials
 A Siddiqui, C Xu, S J Magorrian et al.
- How transparent is graphene? A surface science perspective on remote epitaxy Zachary LaDuca, Anshu Sirohi, Quinn Campbell et al.
- Metal-organic chemical vapor deposition of hexagonal boron nitride: from high-quality growth to functional engineering Seokho Moon, Semi Im, Jawon Kim et al.

2D Materials



OPEN ACCESS

RECEIVED

7 June 2025

REVISED

25 September 2025

ACCEPTED FOR PUBLICATION

3 October 2025

PUBLISHED

17 October 2025

Original Content from this work may be used under the terms of the Creative Commons Attribution 4.0 licence.

Any further distribution of this work must maintain attribution to the author(s) and the title of the work, journal citation and DOI.



PAPER

Solving the phase problem of diffraction: x-ray standing wave imaging on bismuthene/SiC(0001)

Niclas Tilgner^{1,2}, Susanne Wolff^{1,2}, Serguei Soubatch^{3,4}, Tien-Lin Lee⁵, Fabian Göhler^{1,2}, F Stefan Tautz^{3,4,6}, Thomas Seyller^{1,2}, Philip Schädlich^{1,2,*} and Christian Kumpf^{3,4,6,*}

- Chemnitz University of Technology, Institute of Physics, 09126 Chemnitz, Germany
- ² Center for Materials, Architectures and Integration of Nanomembranes (MAIN), 09126 Chemnitz, Germany
- ³ Peter Grünberg Institut (PGI-3), Forschungszentrum Jülich, 52425 Jülich, Germany
 - ⁴ Jülich Aachen Research Alliance (JARA), Fundamentals of Future Information Technology, 52425 Jülich, Germany
- ⁵ Diamond Light Source Ltd, Harwell Science and Innovation Campus, Didcot, Oxfordshire OX11 0DE, United Kingdom
- Experimentalphysik IV A, RWTH Aachen University, 52074 Aachen, Germany
- * Authors to whom any correspondence should be addressed.

E-mail: philip.schaedlich@physik.tu-chemnitz.de and c.kumpf@fz-juelich.de

Keywords: x-ray standing wave imaging, phase problem of diffraction techniques, bismuthene, graphene Supplementary material for this article is available online

Abstract

For establishing a fundamental understanding of the emerging properties of two-dimensional (2D) materials, a reliable determination of the crystallographic structure is essential, as we demonstrate in this work for the specific case of the quantum spin Hall insulator bismuthene. Diffractionbased methods are widely used for structure determination, however, they suffer from a fundamental shortcoming, the phase retrieval problem, that is the inability to directly measure the phase of scattered waves. The normal incidence x-ray standing wave (NIXSW) technique circumvents this problem by introducing a Bragg-generated x-ray standing wave field throughout the sample, relative to which any atomic species can be localized. In essence, a single NIXSW measurement captures the complex scattering factor (amplitude and phase) corresponding to one single Bragg reflection. Collecting data for multiple reflections enables a three-dimensional reconstruction of the scattering density as the Fourier sum of all measured scattering factors. Here, we utilize this technique to reveal the mechanism of a reversible switching process that has been reported for a 2D Bi layer recently (Tilgner et al 2025 Nat. Commun. 16, 6171). In this prominent example, the Bi layer is confined between a 4H-SiC substrate and an epitaxial graphene layer, and can be reversibly switched between an electronically inactive precursor state and the bismuthene state. In our NIXSW imaging experiment, we clearly identify the change of the adsorption site of the Bi atoms, caused by H-saturation of one out of three Si dangling bonds per unit cell, as the key feature leading to the formation of the characteristic band structure of the 2D bismuthene honeycomb.

1. Introduction

Resolving the structure of surfaces, interfaces and thin films at the atomic scale is a fundamental prerequisite for understanding the properties and functionalities of almost any physical system or device. Prominent examples in this context are stacks of two-dimensional materials and van der Waals heterostructures, in particular novel materials with emerging properties, which are in the focus of intense research since the discovery of graphene about two decades ago. For the detailed structure determination in these (and many other) fields, various diffraction methods play a crucial role. However, it is well known that any diffraction experiment suffers from the fact that it can only determine the amplitudes of the scattering factors, since the measured intensities represent the absolute squares of the complex scattering factors, while the phases are lost. If amplitudes and phases of the structure factors

were available, a simple and straightforward Fourier-backtransformation would be possible, resolving the atomic structure of the system in unrivaled clearness, without the necessity of any structural model refinement, and hence without the remaining uncertainty of whether or not the unique 'best structure' has been found in the refinement.

While in the past significant effort was invested in developing suitable workarounds for the phase problem, such as ab initio approaches (so called 'direct methods', see [1-6] and references therein) or the Patterson method [7, 8], there is one very elegant way of determining amplitudes and phases of the scattered waves in crystalline samples, namely the normal incidence x-ray standing wave (NIXSW) technique [9-13]. This technique exploits the interference pattern created by incident and Bragg reflected x-rays, which represents a standing wave field with a period corresponding to the Bragg plane spacing of the used reflection. The atoms within the structure can then be localized with respect to this standing wave field, since they absorb differently strong from the standing wave depending on their positions. The absorption yield is detected via photoelectrons or fluorescence. More details on the NIXSW technique are given in the Methods section.

NIXSW, as described so far, allows the localization of the atomic species in one direction, namely perpendicular to the Bragg planes used to generate the standing wave, i.e. in the direction of the scattering vector $\mathbf{H} = (hkl)$. In most of the recent NIXSW based studies on atomic and molecular adsorbates at surfaces [14-27] and on 2D material heterostacks [28–35], a reflection normal to the surface was used, in order to investigate vertical distances between adsorbates or layers and the substrate. These vertical distances were then interpreted in terms of bonding distances, revealing valuable insights into the nature of chemical interactions at surfaces (e.g. covalent or van der Waals). In some favorable cases, it was possible to obtain also some lateral information, by utilizing reflections with a scattering vector not normal to the surface. This allows, e.g. to determine adsorption sites through triangulation [36-39]. However, this technique is often not feasible, in particular for systems with different surface terminations or multiple adsorption sites.

Nonetheless, the fundamental advantage of this approach is that every single of these 'one dimensional' NIXSW measurements on the scattering vector \boldsymbol{H} in fact provides two parameters, namely amplitude and phase of the $\boldsymbol{H}^{\text{th}}$ (complex) structure factor \mathcal{F}_H of that atomic species, the absorption yield of which was recorded. Since the structure factor \mathcal{F}_H in turn represents the $\boldsymbol{H}^{\text{th}}$ Fourier component of the three-dimensional atomic distribution, a sufficiently complete set of individual NIXSW measurements on

different (inequivalent) Bragg reflections \boldsymbol{H} opens the way to a Fourier analysis of the structure [12, 13, 40, 41]. Hence, the atomic density in the crystal can be reconstructed, simply by calculating the Fourier sum of all experimentally available structure factors. This Fourier-based reconstruction is called 'NIXSW imaging', since it represents a model-free approach yielding a three-dimensional image of the atomic arrangement within the unit cell with sub-Angstrom resolution. NIXSW imaging is capable of revealing intricate structural details in cases when conventional diffraction or microscopy methods may struggle to yield sufficient information, as we will demonstrate for the prominent example of bismuthene on SiC in the following. Note that, although this technique was suggested more than two decades ago [41], it was hardly used owing to the fact that in-vacuum high-precision goniometers for reliable and reproducible sample orientation are required, but were not available until recently.

In this paper, we report an NIXSW imaging experiment on a 2D heterostack consisting of a graphene layer on an intercalated Bi layer on 4H-SiC(0001), a system which at present attracts much attention in the 2D materials community since it is discussed to form the 2D material bismuthene. The quantum spin Hall insulator bismuthene is a potential candidate for next-generation applications in the field of quantum transport or quantum computing, mainly since it exhibits a very large topological band gap that might enable applications at room-temperature [42, 43]. The structural results we obtain in our NIXSW imaging study in fact allowed us to identify the structural key feature that turns the intercalated Bi layer into the 2D honeycomb structure bismuthene.

Contemporary research on confinement heteroepitaxy of Bi beneath epitaxial graphene on SiC(0001) identified two different Bi phases that are formed by intercalation of the graphene buffer layer [28, 44] (which is often referred to as zeroth layer graphene (ZLG) since it is hybridized with the substrate [45–47]). In the intercalation process performed by Bi deposition on the sample surface and sequential annealing at elevated temperatures, at first the Bi α phase is formed with monolayer coverage and, in relation to the substrate's surface unit cell, (1×1) periodicity [28, 44]. At higher temperatures, the Bi density decreases and the $(\sqrt{3} \times \sqrt{3})R30^{\circ}$ -reconstructed β phase is formed.

The latter is the topic of the research presented here. So far, the atomic configuration of the β phase has not yet been determined. On a hexagonal surface, the three most plausible adsorption sites are the ontop site T_1 and the hollow sites T_4 , and H_3 , which correspond to sites above the Si atoms of the first, second, and third SiC bilayer, respectively. Note that

the index refers to the number of next-by neighbors. For the T₁ (short for tetrahedral 1-fold) and the H₃ (hexagonal 3-fold) sites this is obvious, they have one and three Si surface atoms as next neighbors, respectively. The T₄ site also has three Si next neighbors, and additionally the uppermost C atom of the first SiC bilayer as a close-by neighbor, therefore it is called T₄ (short for tetrahedral 4-fold). It was initially suggested that Bi adsorbs on the H₃ hollow sites (Sohn et al [44]), resulting in a structure with only one Bi atom per $(\sqrt{3} \times \sqrt{3})R30^{\circ}$ unit cell, i.e. 1/3 monolayer coverage. But one might also expect a structure similar to that obtained by Reis et al [48], who reported the formation of a Bi honeycomb on a hydrogen terminated SiC surface, which the authors discuss in terms of a bismuthene layer. Our own work [43] shows that hydrogen indeed plays an important role in the formation of bismuthene. While the β phase, as prepared from the α phase, shows no electronic features that would be indicative of 2D bismuthene (as seen in angle resolved photoelectron spectroscopy), the situation changes when the sample is annealed in hydrogen atmosphere. In this case, some of the surface Si dangling bonds, which before hydrogenation can only be saturated by Bi, now become saturated by hydrogen. This changes the electron configuration in the Bi β phase layer and triggers the formation of a honeycomb structure that shows all characteristic features of the quantum spin Hall insulator bismuthene. The decisive aspect in the structure of the Bi layer is a change of the Bi adsorption site from a T₄ hollow to a T_1 top site above the Si atoms, which is detected in our NIXSW imaging study and discussed in detail in this paper.

2. Results and discussion

2.1. Normal incidence x-ray standing wave

The NIXSW technique is element-specific, since the absorption yield can be measured separately for each atomic species (either by fluorescence or x-ray photoelectron spectroscopy (XPS)). Owing to a relatively high energy resolution of modern synchrotron photoemission beamlines one can even separate identical species in different chemical environments. This is essential in our case, because we need to separate bulk-carbon from graphene-carbon. However, a very careful and detailed fitting of the XPS data is required for a proper separation of the individual species. In figures 1(a)–(d) we show representative XP spectra for the three relevant atomic species, namely C1s, Si 2s and Bi $4f_{7/2}$ core levels. Note that the latter two were measured in a single spectrum, due to their similar binding energies. Panels (a) and (b) show the data for the β phase (' β '), panels (c) and (d) for bismuthene (hydrogenated β phase, ' β +H'). For both phases, different fitting models have been used,

according to different configurations of the samples. Note that the fitting models for the XP spectra, in particular that for C1s, were developed in well-established procedures based on spectra with much higher resolution than those measured here at relatively high photon energies. Further details on the models used can be found in Wolff *et al* [28] and (regarding the ZLG) in Emtsev *et al* [49].

When preparing the Bi β phase from an α phase sample, a partial de-intercalation cannot be avoided [28]. This leads to the coexistence of the desired Bi-intercalated quasi-freestanding graphene (QFG) domains with non-intercalated areas, in which only a ZLG is present. These ZLG regions are visible in both C 1s and Si 2s spectra. In the C 1s spectra (figure 1(a)), two side peaks CZLG (red and orange) appear next to the main graphene peak C_{Bi}^{QFG} (blue), and also next to the C 1s bulk peak (C_{Bi}^{bulk} , magenta) a side peak C_{ZLG}^{bulk} (cyan) is seen. Also in the Si 2s spectrum the core level splitting caused by the different structures of ZLG and QFG above can be seen (red and dark green curves in figure 1(b)) [28, 47]. For fitting the Bi $4f_{7/2}$ core level, a single symmetric profile was used, representing the confined insulating Bi layer of the β phase [28, 44]. Further details of these fitting models are discussed in section 1 of the Supplementary Material.

The hydrogenation performed to transform the Bi β phase into bismuthene also affects the ZLG regions of the sample. The ZLG in these areas undergo hydrogen intercalation [45], which transforms them into H-intercalated QFG, and causes significant changes in both the C 1s and the Si 2s spectra. The C^{ZLG} component is replaced by a C^{QFG}_H peak, now at a lower binding energy than that of the C^{OFG}_{Bi} peak, and the bulk carbon appears as one single peak since the difference in the surface band bending between the bulk underneath QFG and the bulk underneath bismuthene cannot be resolved. Furthermore, it is noteworthy that in contrast to the β phase before hydrogenation, the Bi 4f_{7/2} peak is now asymmetric, reflecting the metallic nature of the Bi layer after hydrogenation [43].

In an NIXSW scan, the photon energy is varied in a range of a few eV around the Bragg energy of the applied reflection, in this case the 4H-SiC(0004). In addition to the XP spectra, the Bragg-reflected intensity (so-called 'reflectivity') is also recorded at each energy step during the scan, and typical profiles are plotted as the bottom curve in figures 1(e) and (f). In the photon energy range with non-zero reflectivity, a standing wave field is formed by the interference of the incident and the Bragg-reflected wave. During the scan through the Bragg condition, the phase of this standing wave field changes by π , causing the standing wave to shift by half of the Bragg plane spacing through the crystal. This in turn causes a modulation of the x-ray intensity at the position of any atom in the crystal (and at its surface), which manifests itself as a

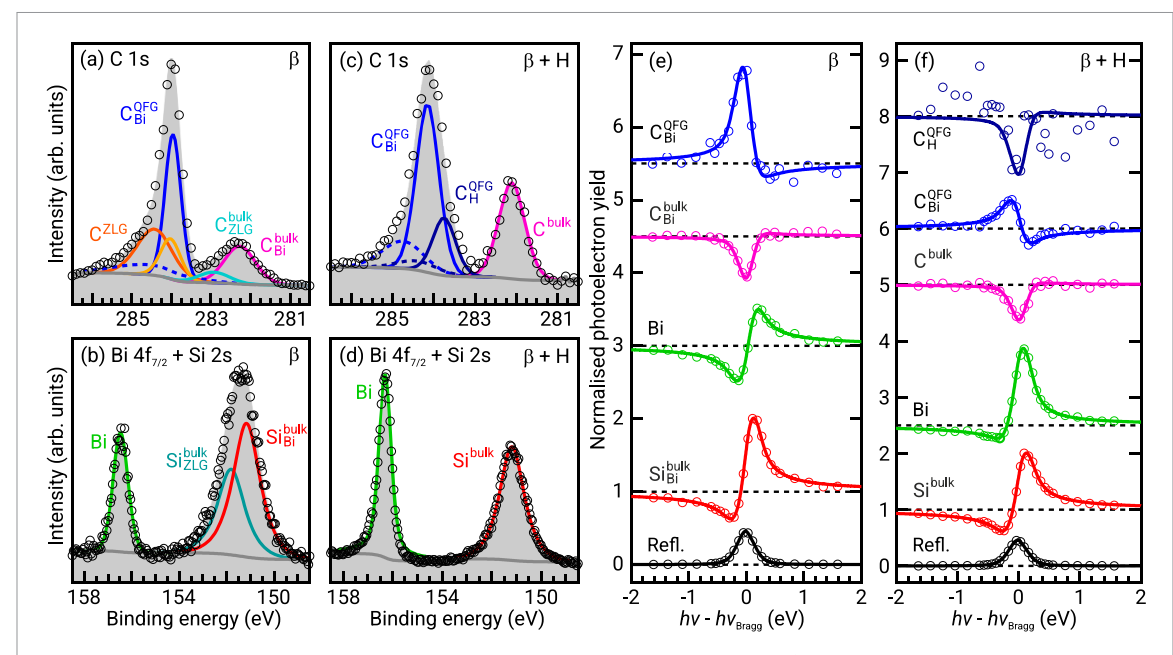


Figure 1. (a), (b) and (c), (d) Representative XP spectra of C 1s, Si 2s and Bi $4f_{7/2}$ of the β phase before, and the bismuthene phase after hydrogenation (β +H), respectively. The spectra were measured at a photon energy \sim 5 eV below the the Bragg energy of the 4H–SiC(0004) reflection ($h\nu_{\text{Bragg}} = 2.4634 \,\text{keV}$). All peaks relevant for the NIXSW analysis are labeled, and further details on the fitting models discussed in section 1 of the Supplementary Material. (e), (f) Corresponding absorption yield curves and typical reflectivity curves of the (0004) reflection for both phases.

modulation of the photoelectron yield. Consequently, recording XP spectra near the Bragg energy and plotting the partial photoelectron yields (for all relevant components) as a function of the photon energy provides photoelectron yield curves that are characteristic for the positions of the corresponding atoms relative to the Bragg planes. In figures 1(e) and (f) we display the yield curves for the two phases under study.

In a conventional NIXSW data analysis, the yield profiles are fitted, together with the reflectivity curve, and two structural parameters are obtained, the so-called coherent position P_c^H and the coherent fraction P_c^H , both taking values between 0 and 1. The former represents the (averaged) position of the considered species w.r.t. the $\mathbf{H}=(hkl)$ Bragg planes and in units of the Bragg plane spacing d_H , while the latter indicates the quality of order of the species. $F_c^H=1$ indicates the case of perfect order (all relevant atoms at the same distance to the Bragg planes), while a value of 0 usually corresponds to complete disorder. In cases when a species obtains several well-defined positions, the situation is more complicated, as will be discussed below.

It should be mentioned that the fitting parameters P_c^H and F_c^H are obtained without any modeling, but are a direct result of the experimental data. For interpretation and illustration, they are often displayed as complex numbers $F_c^H \exp\left(2\pi\,i\,P_c^H\right)$ in a polar diagram, the so-called Argand diagram. Figure 2(a) shows this diagram for the NIXSW results of the β

phase obtained from the experiment on the (004) Bragg reflection ((0004) in the notation for hexagonal lattices, (hkil), with i = -h - k). Each data point represents one individual measurement. We have recorded several data points for each species on different locations on the sample surface. Hence, the small scattering of the data for each species indicates a high sample homogeneity.

For all four species (Si and C in the bulk, Bi and graphene-C at the surface) we find coherent fractions very close to unity. While for the bulk species this is to be expected, for both surface species, Bi and graphene-C, it indicates the adsorption of the atoms at a well-defined height, i.e. in a very flat and unbuckled layer. Hence, the coherent positions can straightforwardly be interpreted as distances between the atomic layers, as illustrated in the balland-stick model of the β phase shown in figure 2(b). Most interestingly, we find a vertical spacing of only 2.24(2) Å between the bulk-terminating Si atoms and the Bi layer, a number significantly smaller than the sum of the covalent radii of the two species (2.67 Å [50]). This distance is not compatible with a vertical covalent Bi-Si bond, making the on-top adsorption of Bi above the uppermost Si very unlikely. It might be compatible with a hollow site adsorption, as will be discussed below. As a second result, the spacing between the Bi layer and graphene was determined to be 3.66(3) Å, a value that is in good agreement with the sum of the corresponding van der Waals radii (3.77 Å [51, 52]), and hence indicates a primarily van

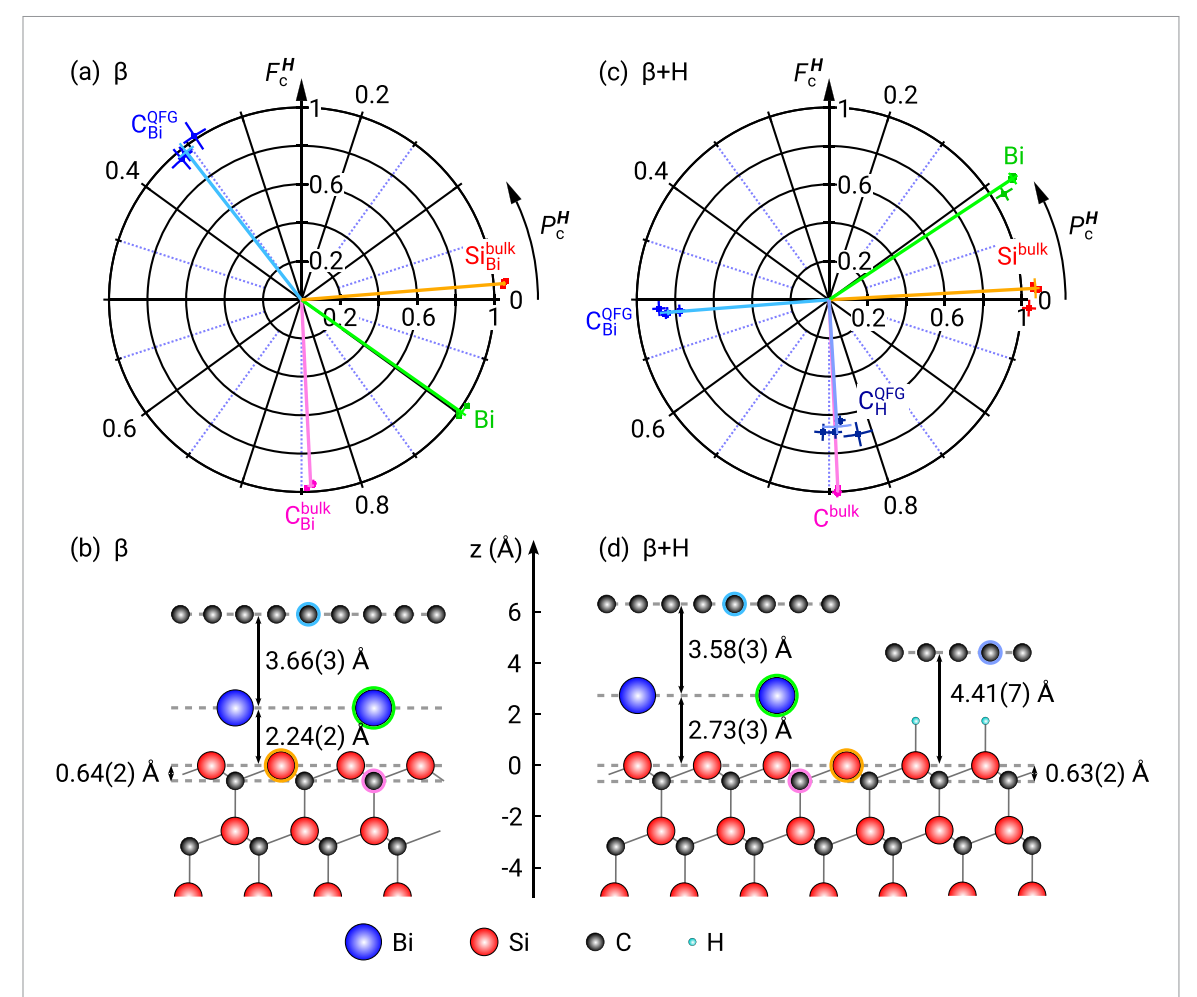


Figure 2. (a) Argand representation of the NIXSW results for the β phase (before hydrogenation), obtained for the (0004) reflection. Each data point represents a complex number with modulus F_c^H and phase P_c^H . Individual data points for each species correspond to several measurements on different sample positions, their average is shown as polar vectors with error bars. (b) Corresponding ball-and-stick model illustrating the vertical distances between the relevant species, derived from the coherent positions. (c), (d) Same like (a), (b), but for the bismuthene phase after hydrogenation. In (d), bismuthene and QFG regions are illustrated in the left and right, respectively.

der Waals-like interaction between these two layers. This is consistent with previous NIXSW studies on Bi-intercalated graphene and other similar systems [28–30].

For the bismuthene phase, the Argand diagram is shown in figure 2(c). The coherent positions of the surface species discussed for the β phase have changed significantly in the hydrogenation process; both became larger by almost the same amount, indicating that the Bi-graphene bilayer moves upwards almost rigidly. In the left part of figure 2(d) the numbers are shown. Bi moved up by $0.49 \,\text{Å}$ to $2.73(3) \,\text{Å}$, a number very close to the covalent bonding distance, and graphene is now only slightly closer to Bi, at a distance of $3.58(3) \,\text{Å}$.

Furthermore, one additional graphene species has been identified for the bismuthene sample, originating from the regions that were originally covered by a ZLG only; they have transformed into H-intercalated (QFG) regions (see discussion above). These regions represent a minority phase with no impact on the bismuthene-covered regions. The C1s component

of the QFG minority phase is much smaller than those of all other species, and hence the corresponding yield curve scatters more strongly. However, the data can be reliably analyzed and result in a height of 4.41(7) Å and a coherent fraction of 0.66(4). Both values closely match those obtained in previous NIXSW studies on hydrogen-intercalated graphene on SiC(0001) (z=4.27 Å and $F_{\rm c}^H=0.68$ [53, 54]). The corresponding ball-and-stick model is shown in the right part of figure 2(d).

The main conclusion of a comparison of the (0004) NIXSW results for the β phase (before hydrogenation) and the bismuthene phase (after hydrogenation) is the increase of the vertical distance between Bi and the uppermost bulk Si atoms from 2.24(2) Å to 2.73(3) Å. This finding is compatible with a change of the Bi adsorption site from a hollow to the on-top site, but from vertical distances alone an unambiguous conclusion is hardly possible. There are too many other factors, as e.g. a possible change in the bonding strength, that may influence the vertical distance. An unambiguous determination of the adsorption

site requires additional lateral information, as it is provided by NIXSW performed on inclined reflections. In the following section we report such measurements, analyzed using the Fourier-based reconstruction of atomic densities called NIXSW imaging, which indeed results in an unambiguous adsorption site determination for Bi in both phases under study.

2.2. Normal incidence x-ray standing wave imaging

As demonstrated above for the (0004) reflection, NIXSW enables the precise determination of atomic positions relative to the Bragg planes with chemical selectivity, since separate measurements for each atomic species can be performed. In case of a single adsorption geometry this is straightforward, since the measured coherent position is directly related to the vertical position (adsorption height) of the atoms. But even in more complex situations, i.e. when multiple adsorption sites are present and this straightforward interpretation does not apply any more, NIXSW still allows a clear structure determination in many cases. The reason for this is that the parameters obtained from a single NIXSW measurement (using the Bragg reflection H), that are the coherent fraction F_c^H and position P_c^H , are directly related to the structure factor \mathcal{F}_H of the structure under study. Strictly speaking, the Argand representation of the NIXSW results corresponds to the normalized species-specific geometrical structure factor \mathcal{F}_H [10–13, 40, 41], i.e.

$$\mathcal{F}_{H} = F_{c}^{H} \exp\left(2\pi i P_{c}^{H}\right). \tag{1}$$

Since \mathcal{F}_H also represents the \mathbf{H}^{th} -order Fourier coefficient of the distribution function $\rho(\mathbf{r})$ of the atomic species considered,

$$\mathcal{F}_{H} = \int_{\mathbb{R}^{C}} \rho(\mathbf{r}) \exp(i\mathbf{H} \cdot \mathbf{r}) d\mathbf{r}. \tag{2}$$

Equations (1) and (2) imply that $\rho(r)$ can be reconstructed from the NIXSW measurements by summing up the Fourier components [10–13, 40, 41]:

$$\rho(\mathbf{r}) = \sum_{\mathbf{H}} \mathcal{F}_{\mathbf{H}} \exp\left(-i\mathbf{H} \cdot \mathbf{r}\right)$$

$$= \sum_{\mathbf{H}} F_{c}^{\mathbf{H}} \exp\left(2\pi i P_{c}^{\mathbf{H}}\right) \exp\left(-i\mathbf{H} \cdot \mathbf{r}\right)$$

$$= 1 + 2 \sum_{\mathbf{H} \neq \mathbf{0}, \ \mathbf{H} \neq -\mathbf{H}} F_{c}^{\mathbf{H}} \cos\left(2\pi P_{c}^{\mathbf{H}} - \mathbf{H} \cdot \mathbf{r}\right). \quad (3)$$

The last simplification introducing the cosine is valid due to Friedel's law, in our case that is $F_c^{-H} = F_c^H$ and $P_c^{-H} = -P_c^H$ [41], and due to $F_c^0 = 1$. Of course, only the infinite sum will result in a complete reconstruction of the distribution function, which is experimentally not feasible. However, in practice it turns out

that—depending on the complexity of the investigated system—measurements on a manageable number of less than 10 symmetrically inequivalent Bragg reflections are sufficient to solve the structure unambiguously. In the present case of the β and bismuthene phases, we have measured seven independent reflections, the (0004), (10 $\overline{1}1$), ($\overline{1}011$), (10 $\overline{1}2$), ($\overline{1}012$), (10 $\overline{1}3$), and ($\overline{1}013$) reflections. Together with their symmetry equivalent reflections (that are the (*ihkl*) and (*kihl*) reflections), this results in a Fourier sum of 19 components. For all reflections we have recorded NIXSW data for all atomic species discussed above. Corresponding yield curves, Argand diagrams, and a table summarizing all the resulting data are shown in section 2 of the Supplementary Material.

2.2.1. NIXSW imaging results for the bulk species

We start the discussion of the results with the bulk species, since these represent an important reference for the adsorbate. Figure 3 shows the reconstructed atomic density distribution for the case that only one Fourier compound is considered (single component analysis). By restricting the sum in equation (3) to the H = (0004) term, a cosinusoidal distribution in z direction is obtained as can be seen in figure 3(a). The maximum lies close to zero on the [0001] axis and has a high amplitude since the coherent position and fraction (phase and amplitude of the cosine term, respectively) were $P_c^{(0004)} = 0.014(2)$ and $P_c^{(0004)} = 1.031(8)$ in the experiment. Further maxima are located at distances of multiples of 2.52 Å, according to the Bragg plane spacing $d_{(0004)}$. Hence, this plot illustrates the vertical structure of the bulk Si species with four Si layers in the unit cell. The density distribution maps for the other reflections (figures 3(b)–(d)) show similar scenarios for their respective direction of the H vector and the corresponding Bragg plane spacing d_H . Smaller amplitudes (i.e. smaller coherent fractions) indicate that not all Si atoms lie at the same distance to the Bragg planes in these directions. Hence, in contrast to the case of the (0004) reflection, here we cannot directly conclude on atomic positions or distances from the individual plots. However, from these plots it becomes clear that lateral structural information is added by the NIXSW measurements on these inclined reflections.

Extending the Fourier sum to all available terms (that are the four shown in figure 3 and 15 others that are not shown) results in the lower right plot in figure 4(a) (labeled 'side view $(1\bar{2}10)$ '). This map represents a cut through the Fourier-reconstructed density distribution map of the Si bulk species in the $(1\bar{2}10)$ plane (spanned by the surface normal [0001] and the [10 $\bar{1}0$] directions). In this plane, the bulk layers A, B and C are oriented horizontally, but are shifted with respect to each other.

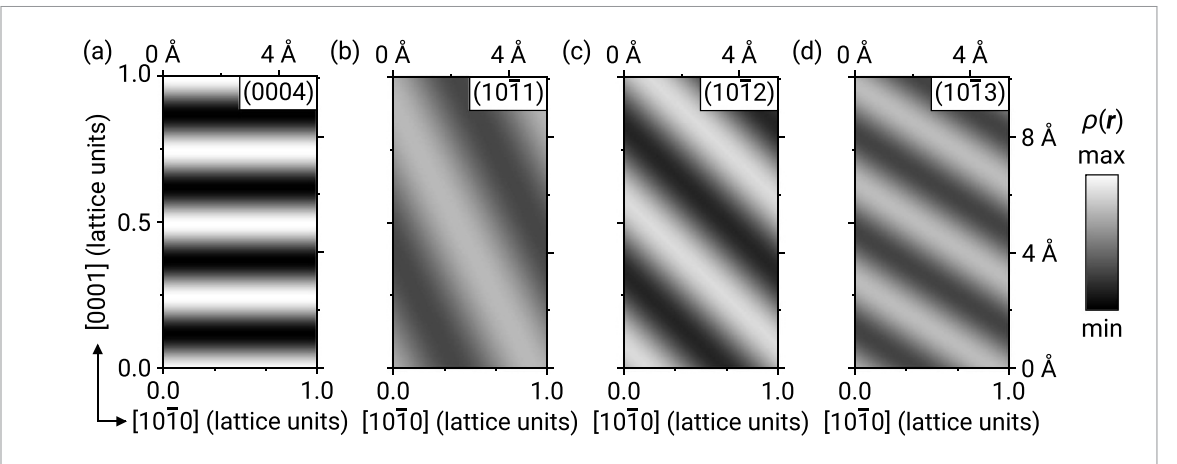


Figure 3. Density distribution maps (2D cuts in the $(1\overline{2}10)$ plane) of selected individual Fourier terms for bulk Si. The distributions correspond to single, one-dimensional cosine functions, the amplitudes and phases of which are given by the coherent fractions and positions obtained for the respective Bragg reflection. The period of the cosine corresponds to the Bragg plane spacing. High (low) densities are shown bright (dark).

The other two maps represent perpendicular planes, namely the (0001) plane (top view onto the unit cell, upper map) and another side view, the $(10\overline{1}0)$ plane (left). The dashed orange lines in the $(1\overline{2}10)$ map indicate the intersection lines of the other two planes.

The interference of the various cosine terms in the Fourier sum produces clearly separated maxima. They indicate the positions of the bulk Si atoms in three dimensions and reproduce the expected structure of the 4H-SiC bulk crystal very well (see superimposed ball-and-stick model in the $(1\overline{2}10)$ projection). Also the lateral shift of neighboring layers in $[10\overline{10}]$ direction according to the ABCBA stacking is reproduced correctly. The same is the case for the bulk C atoms. Figure 4(b) shows the result obtained from the NIXSW data recorded for the C 1s bulk component. In the side views, the patterns of Si and C are very similar, but vertically shifted according to the Si-C bonding distances. When comparing the top-view maps of (a) and (b), one also finds a lateral shift: One species appears at hollow sites of the other. This is due to the z-position of the horizontal cuts, which were chosen within the same bilayer (layer C in this case), as indicated by the dashed orange lines in the $(1\overline{2}10)$ maps. Note that for silicon the maxima of the B layers appear slightly weaker compared to those of the A and C layers, for carbon it is vice versa. This is most likely due to the finite number of Fourier components used in the analysis.

The full 3D structure of the 4H-SiC crystal is obtained when the reconstructed density distributions for both species are combined. In figure 4(c) we present top and side views (the (0001) and $(1\overline{2}10)$

planes, respectively), with the distributions of both species superimposed, Si in red and C in black. The intensity scaling is chosen in a way that only clear maxima of the individual density distributions are visible. Furthermore, for the side view not only the density in the $(1\overline{2}10)$ plane is shown, but additionally from a parallel plane with an offset of a/2. This produces the characteristic '3-dimensional' side view of 4H-SiC, with all atoms within the unit cell being displayed. The varying sizes of the maxima only reflect the intensity differences in the individual density distribution maps reported above, but have no physical meaning.

2.2.2. NIXSW imaging results for Bi

So far we have used the NIXSW data set recorded for the bulk species in order to explain the principle of the NIXSW imaging technique and to demonstrate that the SiC structure can be unambiguously reconstructed by this model-free approach. Now we report the determination of the atomic sites occupied by Bi. In figure 5(a) we show the result obtained for Bi, based on NIXSW imaging data recorded from the Bi 4f_{7/2} core levels. As in figure 4(a), the atomic distribution in the $(1\overline{2}10)$ plane is shown for the β phase prior to hydrogenation. The two strongest maxima that can be seen are located close to the maxima found for the Si bulk species, at coordinates (0.67, 0.22) and (0.67, 0.72) in units of the SiC unit cell, and are labeled 'T₄'. These positions must be interpreted as follows: Since NIXSW imaging is based on the bulk Bragg reflections, it is only possible to determine atomic positions within the periodicity of the bulk unit cell. Atoms within a superstructure are therefore projected into the bulk unit cell. For a surface species, the surface termination of the bulk crystal has to be considered additionally, in order to interpret the obtained positions correctly. In our case, the (0001)-oriented surface of the 4H-SiC bulk exhibits two dominant

⁷ Note that we use the four-index notation to indicate both the Miller-Bravais indices (hkil) and the crystallographic directions in direct space [uvtw]. For direct space directions the commonly used three-index scheme is obtained as [(u-t) (v-t) w].

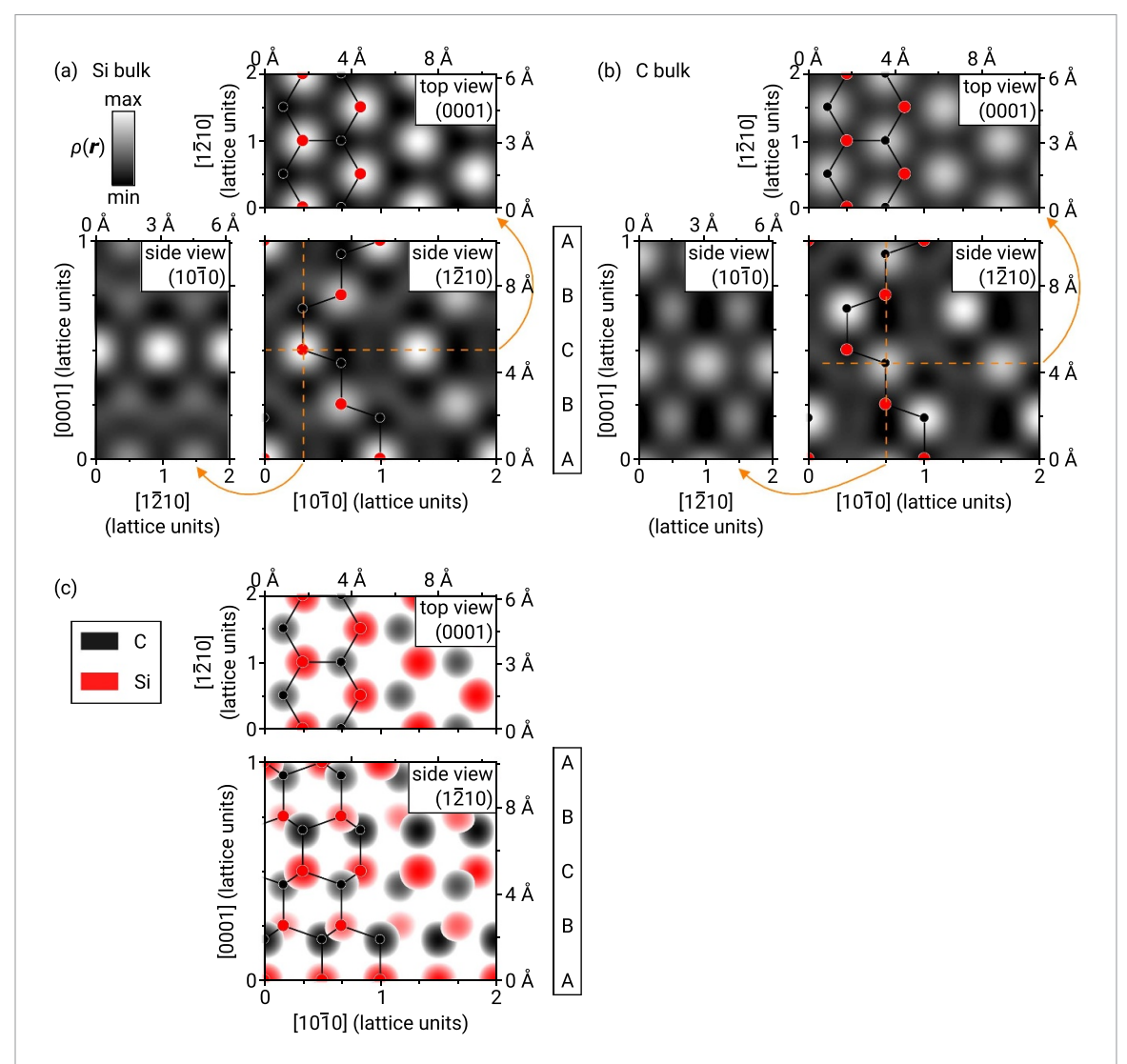


Figure 4. Geometric structure of 4H-SiC as determined by NIXSW imaging. In (a) and (b) selected cross-sectional views of the determined atomic distribution for Si and C, respectively, are shown. The main image (bottom right) displays the $(1\bar{2}10)$ plane, whereas the left and top image show cuts in perpendicular directions as indicated by the orange dashed lines. The superimposed ball-and-stick models demonstrate an excellent agreement between the expected atomic positions and the maxima of the determined atomic distribution. In (c) a combined illustration of the maxima from (a) and (b), color coded as red and black for Si and C, is presented. Note that for the lower image, maxima of an additional plane offset by a/2 were included, to resemble the typical side view of 4H-SiC often shown in ball-and-stick models.

terminations, namely the so called S2 and S2* terminations, which are characterized by the A and C planes forming the surface plane, respectively. Both terminations are indicated by orange dashed lines in figure 5(a). The obtained positions of Bi have now to be interpreted with respect to these surface terminations, which makes clear that the lower of the two Bi peaks must be understood as an adsorbate on the S2 terminated surface, while the upper Bi peak indicates an adsorbate on the S2* termination. Comparing these positions of Bi with those of the bulk species reveals that they are horizontally aligned with the Si atoms in the B layers, hence, they correspond to T₄ hollow sites with a distance of 2.24(2) Å above the bulk-terminating Si plane. Note that there are additional maxima visible in the distribution map, weaker, but still with significant intensity, almost coinciding with the A and C plane. Whether these

are merely artifacts resulting from the limited number of Fourier components, or correspond to Bi atoms on T_4 sites above the (parasitic) $S1/S1^*$ -terminated areas cannot be unambiguously clarified. But the fact that for some of the Bragg reflections, namely the $(10\overline{1}1)$, $(\overline{1}011)$, $(10\overline{1}3)$, and $(\overline{1}013)$ (and their equivalent reflections), the measured coherent fractions were quite small (see section 2 of the Supplementary Material) speaks for the former since this reduces the number of Fourier terms with relevant amplitudes to only seven in this case.

Figure 5(b) illustrates the Bi-based NIXSW imaging results on the bismuthene phase (i.e. after hydrogenation) in a density plot similar to figure 5(a). Here, the primary peaks are clearly shifted, horizontally by precisely \pm 1/3 of the unit cell, and also slightly upwards. The new positions (0.00, 0.27) and (0.33, 0.77) correspond to on-top sites of the terminating Si

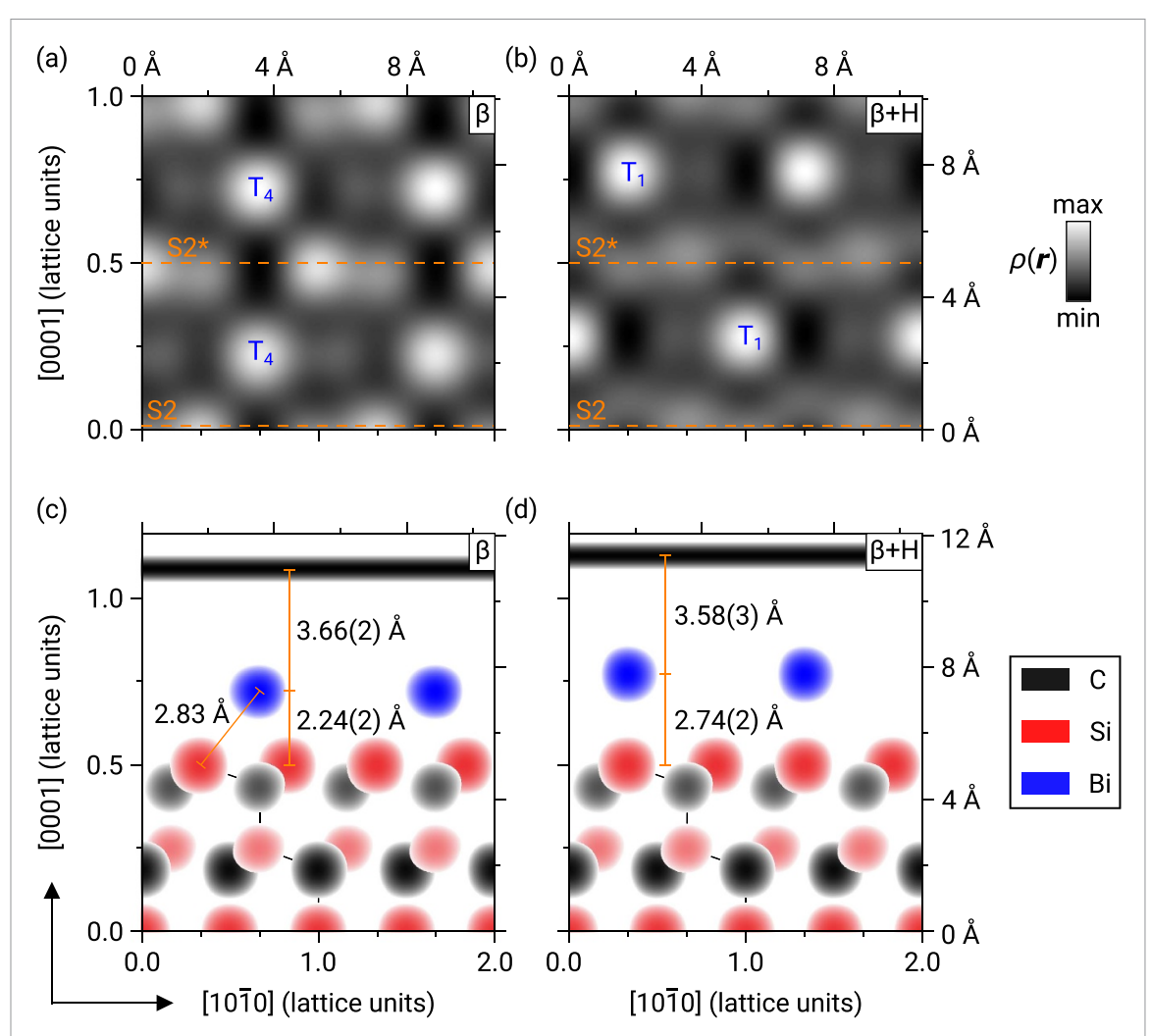


Figure 5. Comparison of the Bi adsorbate structure for both phases, as determined by NIXSW imaging. In (a) and (b) the atomic distributions for Bi are shown for the β phase and bismuthene, respectively (same cross-sectional views as in figures 4(a) and (b)). S2 and S2* terminations of the bulk are indicated by orange dashed lines. In (c) and (d) the combined bulk and surface structure is shown for an S2* terminated surface, with Si, C, and Bi color coded in red, black, and blue, respectively. The change from the T_4 to the T_1 adsorption site due to hydrogenation is clearly visible. For the topmost graphene layer no lateral atomic positions can be determined since it is incommensurate with the substrate.

atoms, i.e. T_1 adsorption sites. The vertical distance between the peak and the surface plane has increased to 2.74(2) Å.

In figures 5(c) and (d) we have combined the NIXSW imaging results for bulk and surface species. For the case of an $S2^*$ terminated surface the uppermost SiC bilayers are shown in a side view in red and black, similar to figure 4(c). The corresponding Bi adsorption sites are added as blue maxima, and the graphene layer is shown as a black bar at the top. For the latter, no lateral positions can be determined, since this layer is incommensurate with the substrate.

These two images clearly illustrate the change of the Bi adsorption site in the phase transition, from the T_4 site in the β phase (above the 2^{nd} -layer Si atoms) to the T_1 site in bismuthene (above the 1^{st} -layer Si atoms). This change of the adsorption site is the decisive structural feature enabling the formation of truly 2D bismuthene (see below and reference [43]). The 3D density maps also allow a straightforward calculation of bonding distances. On the T_4 site, when each Bi atom saturates three Si dangling bonds, we find a length of the inclined Bi-Si bond of 2.83 Å. This value is significantly larger than the sum of the covalent radii for Si and Bi, 2.67 Å [50]. After hydrogenation, when Bi sits on the T_1 on-top site, the Si-Bi bond is stronger with its length reduced to 2.73 Å, close to the expected covalent bond length.

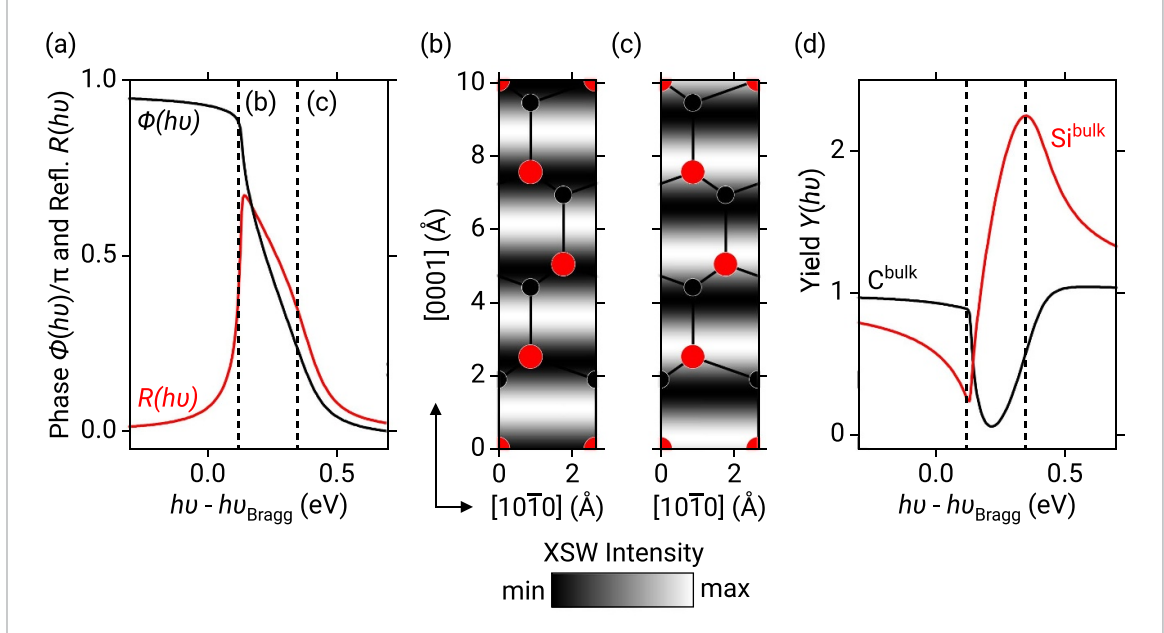


Figure 6. (a) Phase $\Phi(h\nu)$ of the standing wave (black) and sample reflectivity $R(h\nu)$ (red), calculated by dynamical scattering theory for the (0004) reflection of 4H-SiC. (b), (c) Illustration of the corresponding standing wave pattern for two photon energies for $h\nu-h\nu_{\rm Bragg}=0.12$ eV and 0.35 eV, respectively. The energies are indicated by dashed lines in (a). The period of the standing wave corresponds to the Bragg plane spacing. High (low) NIXSW intensities are shown bright (dark). Red and black balls depict the Si and C atoms, respectively. (d) Simulated yield curves for bulk species Si^{bulk} and C^{bulk}.

3. Conclusion

The main result of our comprehensive study of the graphene-protected β and bismuthene phases on the (0001) oriented 4H-SiC surface is the determination of the adsorption site of Bi in both phases. We find that it changes from the T_4 hollow site in the β phase to the T₁ on-top site in bismuthene. This change implies a different coordination of Bi with the underlying top-most Si atoms. At the T₄ hollow site, each Bi atom has three equidistant Si neighbours and thus saturates three dangling bonds. But in the hydrogenation process, Bi is depleted from the hollow site, since hydrogen, with its higher electron affinity, saturates one third of all dangling bonds of the Si atoms. At the same time, Bi moves to an on-top site and forms only one bond to the Si atom underneath (T1 ontop adsorption site). The single Bi-Si bond moves the p_z orbital of Bi, one of its five valence orbitals, away from the Fermi edge. This so-called orbital filtering allows an in-plane hybridization of the remaining four valence orbitals, leading to the formation of a flat honeycomb structure with a graphene-like inplane bonding configuration and to the distinct Dirac-like bands that we observe [43]. This structure is energetically very stable since (i) all Si dangling bonds are saturated by covalent single bonds, 1/3 of them by H, the other 2/3 by Bi, and (ii) the orbital filtering enables the formation of the graphene-like Bi-honeycomb structure. Most likely, this also prevents the system from fully depleting Bi from the Si on-top sites. In case

of a full hydrogenation of the SiC surface, i.e. when all Si bonds were saturated by H, a freestanding Bi layer might be able to form. Theoretical studies suggest that such a freestanding bismuthene layer has a buckled bilayer structure, not a graphene-like inplane bonding configuration [55]. However, freestanding bismuthene in a flat honeycomb arrangement has never been reported and does not seem to be a stable configuration. We conclude that the orbital filtering of Bi and the associated change of the adsorption site represent the fundamental mechanism that leads to the formation of bismuthene.

The key finding of this study was obtained from NIXSW imaging, a method that was suggested more than two decades ago, but hardly applied since then. Unlike all standard diffraction methods, NIXSW can retrieve not only the amplitudes but also the phases of the structure factors [40, 41], and hence allows the precise localization of atomic sites relative to the Bragg planes, independently for all atomic species. The technique is model-free, i.e. no model refinement has to be performed, and hence is not prone to false predictions due to local minima in the goodness-of-fit function, as it is in principal the case for any structure refinement technique. Instead, the element-specific, three-dimensional atomic distribution is obtained simply as the Fourier-sum of the complex structure factors (amplitudes and phases) that were experimentally obtained for a certain set of Bragg reflections. In general, the reconstruction is the better the more Fourier components can be

obtained, and is limited to the bulk unit cell since it is based on bulk Bragg reflections. The latter limitation—in practice—is not a crucial shortcoming, as long as the superstructure unit cell of the investigated surface structure is not too large (see section 4 of the Supplementary Material for details). Under this condition, NIXSW imaging is a very useful, reliably and unique tool for (surface) structure determination, as we demonstrated here for the prominent example of the QSHI bismuthene.

4. Methods

4.1. Sample preparation

4H-SiC wafer pieces were purchased from Pam-Xiamen. The epitaxial graphene synthesis was carried out using the polymer-assisted sublimation growth, which is described in detail elsewhere [56]. Bi was intercalated using an in situ deposition and annealing approach, as reported in previous studies [28, 44]: The deposition was performed in a dedicated evaporation chamber with a base pressure below $5 \times$ 10⁻⁹ mbar, using a custom-built Knudsen cell heated to 550 °C for 120 min. Subsequent to in-vacuo transfer to the ultra-high vacuum (UHV) analysis chamber, the preparation of the α phase by Bi intercalation was executed by heating the sample to 450 °C for 30 min. The β phase transformation was accomplished by additional annealing to 950 °C for 20 min. A pyrometer was used to monitor the temperature, assuming a sample emissivity of 0.9. After brief transport through air, hydrogen intercalation was performed using a contactless infrared heating system by annealing the sample at 550 °C under ultra-pure hydrogen atmosphere (880 mbar, 0.9 slm) for 90 min.

4.2. Normal incidence x-ray standing wave

For an NIXSW experiment the sample is positioned in a monochromatic x-ray beam in a way that the Bragg condition for a certain reflection *H* of the bulk crystal is met. We performed these experiments at a Bragg angle close to 90° (NIXSW). As calculated from dynamic scattering theory, the amplitude and phase of the Bragg-reflected wave (relative to the incident wave) are plotted in figure 6(a) as red and black curves, respectively, for the case of the (0004) reflection of 4H-SiC. In a photon energy scan through the Bragg condition, as it is performed in an NIXSW measurement, the amplitude, usually referred to as reflectivity $R(h\nu) = \frac{I^H(h\nu)}{I_0}$, i.e. the normalized intensity of the reflected wave, shows a peak of finite width, and the phase $\Phi(h\nu)$ changes by π . The standing wave field, formed by interference of the incoming and the Bragg reflected wave, is illustrated in figures 6(b) and (c) for two different photon energies in the left and in the right of the reflectivity profile, see dashed lines in (a). The figures illustrate that the change of the phase between these two energies causes a shift of the standing wave through the crystal, the maxima move from

a position between the Bragg planes (panel (b), $\Phi(h\nu)$ close to π) to a position on the Bragg plane (panel (c), $\Phi(h\nu)$ approaching zero).

This shift of the standing wave represents the key for a localization of the atomic species in the crystal and at its surface. The photoabsorption of any atom scales linearly with the intensity of the standing wave field at its position. Hence, the absorption yield $Y(h\nu)$, which can be measured in a secondary process as, e.g. photoelectron emission or fluorescence, shows an photon-energy dependence that is characteristic for the position of the absorber relative to the diffraction planes of the used Bragg reflection. Figure 6(d) shows simulated yield profiles for the bulk species Si and C atoms: At the photon energy corresponding to (b), the Si atoms lie in a node of the standing wave field, the yield curve therefore shows a minimum, while at the higher photon energy (c), when the Si atoms lie on antinodes, it shows a maximum. An animated version of figure 6 is available in the Supplementary Material. Further details on NIXSW can be found in section 4 of the Supplementary Material and in references [10–13, 57, 58].

All experiments presented in this work were performed at the I09 beamline of the Diamond Light Source Ltd (Didcot, UK) under UHV conditions. The samples were transported to the beamline under UHV conditions after being prepared at the TU Chemnitz. Once the samples were transferred and outgassed, they were positioned in the x-ray beam in a way that the Bragg condition for one specific reflection was met in near-normal-incidence geometry. Note that in order to separate the back-diffracted xray beam from the incident x-ray beam, the experiments were conducted in a slightly off-normal incidence geometry (3.5°) . Then, we scanned the photon energy within a small energy range of ± 1.5 eV around the Bragg energy. For each energy step, the XP spectra of C 1s, Si 2s, and Bi $4f_{7/2}$ as well as the intensity of the back-diffracted x-ray beam were recorded. A Scienta EW4000 HAXPES hemispherical electron analyzer was used to detect the photoelectrons. Analyzing the XP spectra and extracting the intensities of the relevant core level peaks resulted in one photoelectron yield curve per species. The XP spectra were analyzed using CasaXPS [59], while the reflectivity and yield curves were fitted using the NIXSW analysis software Torricelli [57]. In particular, the yield curves were fitted by the function

$$Y(h\nu) = 1 + S_{R}R(h\nu) + 2|S_{I}|\sqrt{R(h\nu)}F_{c}^{H}\cos(\Phi(h\nu) -2\pi P_{c}^{H} + \psi).$$

$$(4)$$

 $S_{\rm R}$ and $S_{\rm I} = |S_{\rm I}|e^{-i\psi}$ denote parameters for the correction of nondipolar effects in the photoemission process, under consideration of the deviation from normal incidence. For details see [57, 58]. This procedure was repeated for all selected Bragg reflections, resulting in a full NIXSW imaging data set,

the analysis of which is explained in the main text. The samples were maintained at room temperature throughout the entire measurements. At normal incidence to the surface (i.e. for the (0004) reflection), the x-ray beam spot size was $400\,\mu\text{m} \times 400\,\mu\text{m}$, and enlarged according to the respective incidence angle for the inclined reflections.

Data availability statement

The data that support the findings of this study are openly available at the following URL/DOI: https://doi.org/10.26 165/JUELICH-DATA/ZJVFIP [60].

Acknowledgments

The authors thank Christoph Lohse for his contributions to substrate preparation. We also thank the Diamond Light Source for granting access to beamline I09 under proposal SI36085-2 and extend our appreciation to the I09 beamline staff (Pardeep Kumar Thakur and Dave McCue) for their valuable support. This work was supported by the German Research Foundation (Deutsche Forschungsgemeinschaft, DFG) within the Research Unit FOR5242 (Project 449119662) and the Collaborative Research Centre SFB-1083 (Project A12).

Author contributions

The project was conceived by N T, T S, P S, and C K. Samples were prepared by N T and experiments performed by N T, S W, S S, T-L L, and C K. The data analysis was performed by N T and S W, and discussed with S S and C K. The model explaining the phase transition was developed by N T, F S T, T S, P S, and C K, and discussed with all authors. Figures were prepared by N T, S W, and S S, and the paper written by N T, F G, P S, and C K.

ORCID iDs

References

- [1] Fienup J R 1982 Appl. Optics 21 2758-69
- [2] Marks L D, Bengu E, Collazo-Davila C, Grozea D, Landree E, Leslie C and Sinkler W 1998 Surf. Rev. Lett. 05 1087–106
- [3] Marks L D, Erdman N and Subramanian A 2001 J. Phys.-Condens. Mat. 13 10677

- [4] Kumpf C et al 2001 Phys. Rev. B 64 075307
- [5] Elser V 2003 J. Opt. Soc. Am. A 20 40-55
- [6] Oszlányi G and Süto A 2004 Acta Crystallogr. A 60 134-41
- [7] Patterson A L 1934 Phys. Rev. 46 372-6
- [8] Rossmann M G and Arnold E 2006 Patterson and Molecular-Replacement Techniques (International tables for Crystallography vol B) ch 2.3, pp 235–63
- [9] Batterman B W 1969 Phys. Rev. Lett. 22 703
- [10] Zegenhagen J 1993 Surf. Sci. Rep. 18 202-71
- [11] Vartanyants I and Kovalchuk M 2001 Rep. Prog. Phys. 64 1009–84
- [12] Woodruff D P 2005 Rep. Prog. Phys. 68 743
- [13] Zegenhagen J and Kazimirov A 2013 x-ray Standing Wave Technique: Principles and Applications (World Scientific Publishing Company)
- [14] Ding P et al 2023 J. Phys. Chem. C 127 20903-10
- [15] Grossmann L, Duncan D A, Jarvis S P, Jones R G, De S, Rosen J, Schmittel M, Heckl W M, Björk J and Lackinger M 2022 Nanoscale Horiz. 7 51–62
- [16] Brülke C $\,et\,al$ 2019 Phys. Rev. B $\,{\bf 99}$ 121404
- [17] Blowey P J, Rochford L A, Duncan D A, Warr D A, Lee T L, Woodruff D P and Costantini G 2017 Faraday Discuss. 204 97–110
- [18] Stadtmüller B, Schröder S and Kumpf C 2015 J. Electron Spectrosc. 204 80–91
- [19] Kleimann C, Stadtmüller B, Schröder S and Kumpf C 2014 J. Phys. Chem. C 118 1652–60
- [20] Goiri E, Matena M, El-Sayed A, Lobo-Checa J, Borghetti P, Rogero C, Detlefs B, Duvernay J, Ortega J E and de Oteyza D G 2014 Phys. Rev. Lett. 112 117602
- [21] Stadtmüller B, Gruenewald M, Peuker J, Forker R, Fritz T and Kumpf C 2014 J. Phys. Chem. C 118 28592–602
- [22] Woodruff D P 2010 J. Phys.-Condens. Mat. 22 084016
- [23] Stadler C, Hansen S, Kröger I, Kumpf C and Umbach E 2009 Nat. Phys. 5 153–8
- [24] Woolley R, Martin C, Miller G, Dhanak V and Moriarty P 2007 Surf. Sci. 601 1231–8
- [25] Schulte K, Woolley R, Wang L, Moriarty P, Birkett P, Kroto H and Cowie B 2005 Nucl. Instrum. Meth. A 547 208– 15
- [26] Gerlach A, Schreiber F, Sellner S, Dosch H, Vartanyants I A, Cowie B C C, Lee T L and Zegenhagen J 2005 Phys. Rev. B 71 205425
- [27] Woolley R A J, Schulte K H G, Wang L, Moriarty P J, Cowie B C C, Shinohara H, Kanai M and Dennis T J S 2004 Nano Lett. 4 361–4
- [28] Wolff S, Hutter M, Schädlich P, Yin H, Stettner M, Wenzel S, Tautz F S, Bocquet F C, Seyller T and Kumpf C 2024 New J. Phys. 26 103009
- [29] Schädlich P et al 2023 Adv. Mater. Interfaces 10 2300471
- [30] Lin Y R, Wolff S, Schädlich P, Hutter M, Soubatch S, Lee T L, Tautz F S, Seyller T, Kumpf C and Bocquet F C 2022 Phys. Rev. B 106 155418
- [31] Lin Y R, Bagchi M, Soubatch S, Lee T L, Brede J, Bocquet F C, Kumpf C, Ando Y and Tautz F S 2021 Phys. Rev. B 104 054506
- [32] Brülke C, Heepenstrick T, Humberg N, Krieger I, Sokolowski M, Weiß S, Tautz F S and Soubatch S 2017 J. Phys. Chem. C 121 23964–73
- [33] Farwick zum H F H et al 2016 ACS Nano 10 11012–26
- [34] Emery J D, Detlefs B, Karmel H J, Nyakiti L O, Gaskill D K, Hersam M C, Zegenhagen J and Bedzyk M J 2013 Phys. Rev. Lett. 111 215501
- [35] Busse C et al 2011 Phys. Rev. Lett. 107 036101
- [36] Kilian L, Weigand W, Umbach E, Langner A, Sokolowski M, Meyerheim H L, Maltor H, Cowie B C C, Lee T and Bäuerle P 2002 Phys. Rev. B 66 075412
- [37] Raths M, Schott C, Knippertz J, Franke M, Lin Y R, Haags A, Aeschlimann M, Kumpf C and Stadtmüller B 2021 Phys. Rev. Mater. 5 094001
- [38] Sugiyama M, Maeyama S and Oshima M 1996 Appl. Phys. Lett. 68 3731–3

- [39] Woicik J, Franklin G, Liu C, Martinez R, Hwong I-S, Bedzyk M, Patel J and Golovchenko J A 1994 Phys. Rev. B 50 12246
- [40] Bedzyk M J and Materlik G 1985 Phys. Rev. B 32 6456-63
- [41] Bedzyk M J, Fenter P, Zhang Z, Cheng L, Okasinski J S and Sturchio N C 2004 Synchrotron Radiat. News 17 5–10
- [42] Gehrig L, Schmitt C, Erhardt J, Liu B, Wagner T, Kamp M, Moser S and Claessen R 2025 *Adv. Mater.* 37 2502412
- [43] Tilgner N et al 2025 Nat. Commun. 16 6171
- [44] Sohn Y, Jung S W, Göhler F, Shin W J, Cha S, Seyller T and Kim K S 2021 *J. Korean Phys. Soc.* **78** 157–63
- [45] Riedl C, Coletti C, Iwasaki T, Zakharov A A and Starke U 2009 Phys. Rev. Lett. 103 246804
- [46] Briggs N et al 2020 Nat. Mater. 19 637-43
- [47] Emtsev K V et al 2009 Nat. Mater. 8 203-7
- [48] Reis F, Li G, Dudy L, Bauernfeind M, Glass S, Hanke W, Thomale R, Schäfer J and Claessen R 2017 Science 357 287–90
- [49] Emtsev K V, Speck F, Seyller T, Ley L and Riley J D 2008 Phys. Rev. B 77 155303

- [50] Pyykkö P and Atsumi M 2009 Chem.-Eur. J. 15 186-97
- [51] Bondi A 1964 J. Phys. Chem. A 68 441–51
- [52] Mantina M, Chamberlin A C, Valero R, Cramer C J and Truhlar D G 2009 J. Phys. Chem. A 113 5806–12
- [53] Sforzini J et al 2015 Phys. Rev. Lett. 114 106804
- [54] Sforzini J et al 2016 Phys. Rev. Lett. 116 126805
- [55] Huang Z Q, Chuang F C, Hsu C H, Liu Y T, Chang H R, Lin H and Bansil A 2013 Phys. Rev. B 88 165301
- [56] Kruskopf M et al 2016 2D Mater. 3 041002
- [57] Bocquet F, Mercurio G, Franke M, Van Straaten G, Weiß S, Soubatch S, Kumpf C and Tautz F S 2019 Comput. Phys. Commun. 235 502–13
- [58] van Straaten G, Franke M, Bocquet F C, Tautz F S and Kumpf C 2018 J. Electron Spectrosc. 222 106–16
- [59] Fairley N et al 2021 Appl. Surf. Sci. 5 100112
- [60] Tilgner N et al 2025 Jülich DATA (https://doi.org/10.26 165/ JUELICH-DATA/ZJVFIP)